Classical and quantum chaos in a circular billiard with a straight cut

Suhan Ree and L. E. Reichl
Center for Studies in Statistical Mechanics and Complex Systems, The University of Texas at Austin, Austin, Texas 78712
(Received 7 July 1998; revised manuscript received 12 March 1999)

We study classical and quantum dynamics of a particle in a circular billiard with a straight cut. Classically, this system can be integrable, nonintegrable with *soft chaos*, or nonintegrable with *hard chaos* as we vary the size of the cut. We plot Poincaré surfaces of section to study chaos. Quantum mechanically, we look at Husimi plots, and also use the quantum web, the technique primarily used in spin systems so far, to try to see differences in quantum manifestations of soft and hard chaos. [S1063-651X(99)06508-3]

PACS number(s): 05.45.Mt, 03.65.Ge, 02.70.Pt

I. INTRODUCTION

In recent years, the dynamics of noninteracting particles in two-dimensional (2D) billiards has been studied in many different geometries [1–6]. Billiards here are assumed to have hard boundaries, and the geometry of a given boundary can solely decide the dynamics of particles inside. Thus, by changing the shape of a billiard, the classical system can be integrable or nonintegrable, and chaos arises in nonintegrable systems. There are two distinct types of chaotic behavior, ''hard chaos'' and ''soft chaos.'' Systems whose dynamics consists of a mixture of stable and unstable periodic orbits are said to exhibit soft chaos. If all periodic orbits in a system are unstable throughout, the behavior is called hard chaos [7]. While soft chaos is more generic, hard chaos is global and has ergodicity. The Poincaré surface of section (PSS) is a good way to observe these behaviors. In PSS, cases with soft chaos will show mixtures of island chains and chaotic regions, and cases with hard chaos will show global chaos. On the other hand, quantum versions of closed billiards have discrete energy spectra, and chaos manifests itself in quantum billiards in indirect ways. The Husimi function of a quantum eigenstate can show a similar pattern with the corresponding PSS when the area of the pattern is bigger than the Planck constant h [8,9]. The statistics of energy-level spacings for classically integrable systems is different from that for strongly chaotic systems [2–5,10–13], and this difference in statistics is commonly used as a signature of underlying chaos.

In this paper, we study the classical and quantum dynamics of a particle in a closed circular billiard with a straight cut (see Fig. 1). We introduce a dimensionless parameter $w = W/R$ to characterize the system where W is the width of the billiard and R is the radius. As we change the size of the cut by varying w, the classical system shows integrability, nonintegrability with soft chaos, and nonintegrability with hard chaos. We will study the manifestations of these classical behaviors in the quantum systems using a diagnostic tool that has proven successful for spin systems, the *quantum web* [13–16].

The quantum web is a quantum analog of a 2D classical action space in which an orbit for an integrable system is represented by a point, (J_1, J_2), where J_1 and J_2 are the actions associated with two degrees of freedom. This analysis is useful when a system has a parameter that can gradually change the system from integrable to nonintegrable. (This makes our billiard a good candidate for analysis in terms of the quantum web.) This transition occurs when a parameter breaks a continuous symmetry. Then, classically, one constant of motion gets broken to make the system nonintegrable. In quantum language, an operator $\hat{A}$, the generator of that symmetry, no longer commutes with the Hamiltonian operator $\hat{H}$. Even when we cannot have simultaneous eigenstates of $\hat{H}$ and $\hat{A}$, the quantum web uses eigenvalues of $\hat{H}$ and expectation values of $\hat{A}$ with respect to eigenstates of $\hat{H}$ to form points in a 2D space. (When the system is integrable, eigenvalues of $\hat{H}$ and $\hat{A}$ for simultaneous eigenstates form points in that space.) Because it deals with not only energy eigenvalues but also values for another operator, the quantum web has more information than energy statistics. In quantum webs, we expect that hard and soft chaos can be distinguished qualitatively.

In Sec. II, we study the classical billiard for integrable and nonintegrable cases, and plot PSS's as we change w in classical mechanics. In Sec. III, we calculate the quantum web using about 100 lowest-energy eigenstates, and observe patterns for classically different cases. The Husimi function [17,18] that extracts the quantum Poincaré section from a quantum state is also calculated for some selected energy eigenstates to examine the quantum web closely.

II. THE CLASSICAL BILLIARD

In this section, we focus on the classical dynamics of the billiard. We define M_w as a circular disk with a straight cut with width $W = wR$. For example, M_2 is a full circle and M_1

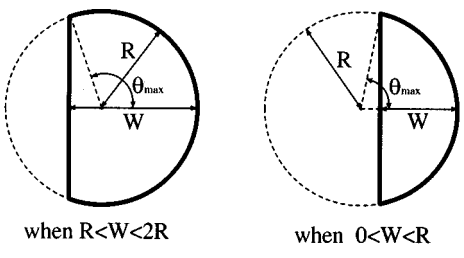

FIG. 1. Geometry of the billiard. When $W = 2R$, it is a full circle, and when $W = R$, it is a half circle. Here $\theta_{\max}$ is given by the equation $\cos\theta_{\max} = (R - W)/R$.

is a half-circle, and w is in the range of $0<w\leqslant 2$. The classical Hamiltonian of a particle inside M_w, using polar coordinates (r,θ), is

$$H_w(r,\theta,p_r,p_\theta)=\frac{p_r^2}{2m}+\frac{p_\theta^2}{2mr^2}+V_w^R(r,\theta), \tag{1}$$

where $V_w^R(r,\theta)$ represents the hard-wall potential of the billiard with radius R and width $W=wR$. To begin, we will study the full circle (M_2) and the half-circle (M_1). Both of these cases are integrable. Then nonintegrable cases will be examined.

A. Full-circle billiard, M_2

The dynamics of a particle inside M_2 is integrable because there are two constants of motion, the energy E and the angular momentum p_θ. Given E and p_θ, the orbit lies on a 2D torus (2-torus) in phase space. There exists a canonical transformation to action-angle variables, $(J_r,J_\theta,\phi_r,\phi_\theta)$, where actions are given by

$$J_r=\sqrt{\frac{2mE}{\pi}}\left[\sqrt{R^2-\frac{p_\theta^2}{2mE}}-\frac{|p_\theta|}{\sqrt{2mE}}\cos^{-1}\left(\frac{|p_\theta|}{R\sqrt{2mE}}\right)\right], \tag{2}$$

$$J_\theta=p_\theta,$$

with the new Hamiltonian $H'=E(J_r,J_\theta)$. We can also find the angle variables (note that ϕ_θ is not equal to θ). We can find explicit expressions of angular frequencies $\dot{\phi}_r=\omega_r$ and $\dot{\phi}_\theta=\omega_\theta$ as functions of E and p_θ using Eq. (2),

$$\omega_r=\dot{\phi}_r=\frac{\partial E}{\partial J_r}=\left(\frac{\partial J_r}{\partial E}\right)^{-1}=\frac{2\pi E}{\sqrt{2mER^2-p_\theta^2}}, \tag{3}$$

$$\omega_\theta=\dot{\phi}_\theta=\frac{\partial E}{\partial J_\theta}=-\left(\frac{\partial J_r}{\partial J_\theta}\right)\left(\frac{\partial J_r}{\partial E}\right)^{-1}$$

$$=\frac{\mathrm{sgn}(p_\theta)}{\pi}\ \omega_r(E,p_\theta)\cos^{-1}\left(\frac{|p_\theta|}{R\sqrt{2mE}}\right). \tag{4}$$

It is useful to look at periodic orbits (orbits for which the ratios of two angular frequencies are rational). We classify periodic orbits using the notation (m,n), where m and n are relatively prime positive integers defined by

$$\left|\frac{\omega_\theta}{\omega_r}\right|=\frac{1}{\pi}\cos^{-1}\left(\frac{|p_\theta|}{R\sqrt{2mE}}\right)=\frac{m}{n}, \tag{5}$$

where $2m<n$ [see Fig. 2(a)]. If we have a periodic orbit classified as (m,n), an infinite number of rotated periodic orbits also belong to (m,n). Therefore, periodic orbits in the full circle are *nonisolated* [1]. For any periodic orbit classified as (m,n), there are n bounces and m revolutions in one cycle. On the other hand, a nonperiodic orbit will not come back to the starting point, and eventually fill the whole 2-torus in phase space.

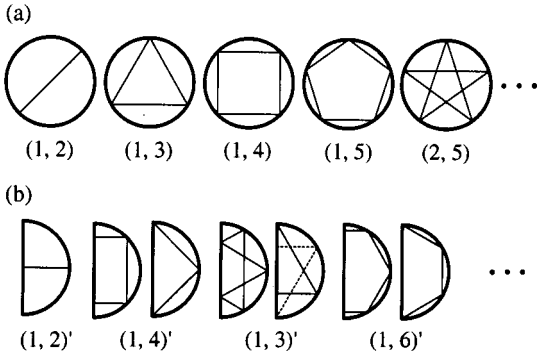

FIG. 2. Closed orbits in integrable cases. (a) In a full circle, periodic orbits can be classified as (m,n) where orbits have m bounces and n revolutions in a cycle. (b) In a half circle, we can use the notation of a full circle to classify periodic orbits as $(m,n)'$.

B. Half-circle billiard, M_1

For the half-circle, we still have two constants of motion, E and p_θ^2. The range of θ is reduced to a half, $-\pi/2<\theta<\pi/2$, but we can still construct 2-tori on which orbits lie. For any orbit in M_1 there is a corresponding orbit in M_2. (If there is an orbit in M_2, folding M_2 in half gives us a corresponding orbit in M_1.) Hence we can use the results found for M_2 to describe some periodic orbits. A periodic orbit is classified as $(m,n)'$ when the corresponding orbit in M_2 is (m,n). Unlike M_2, periodic orbits in M_1 are *isolated*, since there is no rotational symmetry. In the group $(m,n)'$, there are an infinite number of different periodic orbits, but only a few play an important role when w is slightly less than 1. In Fig. 2(b), those periodic orbits are shown. The stabilities of these periodic orbits are all neutral (neither stable nor unstable) like those in M_2.

It is useful to see periodic orbits in the space of E and $|p_\theta|$. A point in this space corresponds to a group of orbits with constants of motion E and p_θ^2. When Eq. (5) is satisfied, the group consists of periodic orbits. Thus the condition to have periodic orbits is given by Eq. (5), and is plotted in Fig. 3. Curves from these conditions are densely populated in the classically allowed region. The classically forbidden region in this space is given by $E-p_\theta^2/(2mR^2)<0$. In integrable cases, orbits are at a point (zero-dimensional) in $(E,|p_\theta|)$ space since E and p_θ^2 are conserved, but as the rotational symmetry breaks by changing w, p_θ^2 is no longer conserved and orbits become one-dimensional. We will see later that Eq. (5) gives us the condition for primary resonances when w is slightly less than 1.

C. M_w when $0<w<1$ or $1<w<2$

Except for the two cases studied above ($w=1,2$), the system is nonintegrable, because E is an only constant of motion in the system of two degrees of freedom. The stabilities of periodic orbits in M_w give us one way to understand the dynamical behavior of the system. The simplest periodic orbit for any w is an orbit with two bounces, going back and forth [for example, $(1,2)'$ in Fig. 2(b)]. To calculate the stability of this orbit, we need to imagine a new billiard M_w^2, which is a composite of circular parts of two M_w's facing

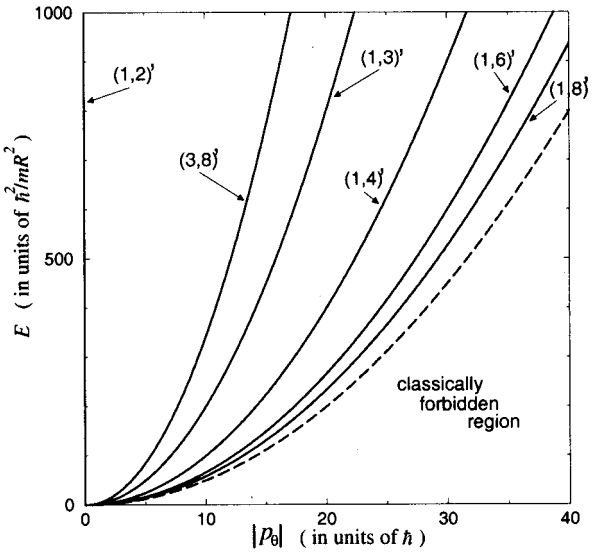

FIG. 3. For a half circle, the condition in $(E,|p_\theta|)$ space to have periodic orbits $(m,n)'$ is given by Eq. (5), and some are plotted. These curves are densely populated in the classically allowed region.

each other. (A billiard of M_w^2 when $0<w<1$ was named the ''lemon'' billiard and studied by Heller and Tomsovic [19].) It is also easy to see that M_1^2 is just M_2. Orbits in M_w have the correspondence with orbits in M_w^2 as orbits in M_1 correspond to orbits in $M_2=M_1^2$. The stability of this two-bounce orbit in M_w^2 can be calculated from a 2×2 matrix $\mathbf{m}$, acting on $(\delta\theta,\delta p_\theta/R\sqrt{2mE})$ on the boundary, which decides the deviation after two bounces [1],

$$\mathbf{m}=\begin{pmatrix} 2(2w-1)^2-1 & 4w(1-2w) \\ 4(2w-1)(1-w) & 2(2w-1)^2-1 \end{pmatrix}. \tag{6}$$

The eigenvalues of $\mathbf{m}$, $\lambda_\pm$, are given in terms of the trace of $\mathbf{m}$,

$$\lambda_\pm=\frac{1}{2}\{\mathrm{Tr}\,\mathbf{m}\pm[(\mathrm{Tr}\,\mathbf{m})^2-4]^{1/2}\}, \tag{7}$$

where we used the relation $\det|\mathbf{m}|=1$, since $\mathbf{m}$ is area-preserving. The orbit is neutral when $|\mathrm{Tr}\,\mathbf{m}|=2$, stable when $|\mathrm{Tr}\,\mathbf{m}|<2$, and unstable when $|\mathrm{Tr}\,\mathbf{m}|>2$. The two-bounce orbit is neutral when $w=0.5$, $w=1$, or $w=2$, stable when $0<w<0.5$ or $0.5<w<1$, and unstable when $1<w<2$. We have seen that all periodic orbits are neutral when the system is integrable ($w=1,2$) but $w=0.5$ is a special case, as we will see later. From this result, we can predict that there are no stable periodic orbits in the billiard $M_{1<w<2}$, and that periodic orbits in $M_{0<w<1}$ are either stable or unstable, except when $w=0.5$. (Ergodicity of the billiard $M_{1<w<2}$ has been proven by Bunimovich [20].) The system shows hard chaos when $1<w<2$ and soft chaos when $0<w<1$.

The Poincaré surface of section (PSS) is one way to observe the chaos. Here PSS is a two-dimensional surface (θ,p_θ) at $r=R$ along the circular boundary $(-\theta_{\max}<\theta<\theta_{\max},\ -R\sqrt{2mE}<p_\theta<R\sqrt{2mE})$. Each orbit gives a point in (θ,p_θ) space every time it touches this surface. Therefore, PSS becomes a 2D area-preserving map. In fully chaotic (ergodic) cases, points generated by an orbit will fill out the whole allowed space in the PSS. In cases of soft chaos, we observe some structure. Some orbits generate island chains and some orbits will fill some remaining regions in a chaotic manner. Since the KAM theorem [7,13] does not apply in this system due to singularities of the boundary, the existence of KAM tori separating island chains is not guaranteed even for small δ when $w=1-\delta$.

In Fig. 4, we show PSS's for various w's. In Fig. 4(a), one orbit is filling the whole region when $w=1.01$. This is a fully chaotic case. Figure 4(b) is an integrable case when $w=1$. When $w=0.99$ [Fig. 4(c)], we see island chains centered at the positions of periodic orbits along with stochastic diffusion in the remaining region. The resonance condition, Eq. (5), gives us locations of island chains. For example, $(1,2)'$ gives us the location $p_\theta/(R\sqrt{2mE})=0$, $(1,4)'$ gives us $p_\theta/(R\sqrt{2mE})=\pm1/\sqrt{2}$, $(1,3)'$ gives us $p_\theta/(R\sqrt{2mE})=\pm0.5$, and $(1,6)'$ gives us $p_\theta/(R\sqrt{2mE})=\pm\sqrt{3}/2$, and so on. As w decreases [Figs. 4(d) and 4(e)], the area of chaotic regions increases although some island chains remain. When $w=0.5$ [Fig. 4(f)], periodic orbits that have neutral stabilities reside in two axes, ($\theta=0$) axis and ($p_\theta=0$) axis. One chaotic orbit starting near the center fills out almost all the surface. As w decreases further, the area occupied by regular orbits grows as we show in Figs. 4(g) and 4(h).

In Fig. 5, we take a different look at PSS. We want to know how the angular momentum at the circular boundary, which is represented by p_θ in Fig. 4, evolves with time at different parts of PSS. We take the upper half of PSS ($-1<\theta/\theta_{\max}<1$, $0<p_\theta/\sqrt{2mE}R<1$), and divide it into 1250 blocks (50 horizontally, 25 vertically). These blocks are numbered $I_p=1,\ldots,1250$ as shown in Fig. 5(a). For each block, we have 100 uniformly distributed initial conditions (points in the block), and calculate the average value of p_θ^2 for the first 50 collisions with the circular boundary for all 100 initial conditions,

$$\langle p_\theta^2\rangle \quad \text{at } I_p=\frac{1}{100}\frac{1}{50}\sum_{i=1}^{100}\sum_{j=1}^{50}p_{\theta(ij)}^2,$$

where $p_{\theta(ij)}$ represents the angular momentum at the jth collision on the circular boundary from the ith initial condition. Then, we have a value of finite-time averaged p_θ^2 for each block represented by I_p, and these values are plotted as a function of I_p for four different values of w. For cases of soft chaos, $w=0.5$ [Fig. 5(b)] and $w=0.9$ [Fig. 5(c)], when blocks are in the regular region of PSS, points behave regularly, and when blocks are in the chaotic region, points behave irregularly. For an integrable case, $w=1.0$ [Fig. 5(d)], the angular momentum is conserved, and the points are regularly placed. For a case of hard chaos, $w=1.5$ [Fig. 5(e)], the position of the block does not matter since the system is ergodic.

The above results again show different behaviors between soft and hard chaos. For cases of soft chaos, time averages of p_θ^2 can have some distinct regular and irregular ranges. On the other hand, for cases of hard chaos, the square roots of time averages of p_θ^2 approach $\sqrt{2mE}R/\sqrt{3}\simeq0.577\sqrt{2mE}R$

regardless of the initial condition as the number of collisions used to calculate the average increases. (The factor $1/\sqrt{3}$ comes from the root mean square of a variable uniformly distributed between -1 and 1.)

III. THE QUANTUM BILLIARD

In this section, we study the quantized M_w billiard using the quantum-web analysis with about 100 lowest-energy eigenstates, and we also look at some individual energy eigenstates using Husimi plots.

A. Numerical method

The Schrödinger equation for this 2D M_w billiard is the Helmholtz equation,

$$(\nabla^2+k^2)\Psi(\mathbf{r})=0, \tag{8}$$

with the Dirichlet boundary condition, $\Psi=0$, on the boundary, $B_w \equiv \partial M_w$, of M_w, where $k^2=2mE/\hbar^2$ and $\nabla^2 = \partial^2/\partial r^2+(1/r)(\partial/\partial r)+(1/r^2)(\partial^2/\partial\theta^2)$ using polar coordinates.

For the classically integrable cases, this equation can be solved analytically. The Hamiltonian $\hat{H}_w$ ($w=1$ or 2) and the angular momentum $\hat{p}_\theta$ ($\hat{p}_\theta^2$ for the half circle) commute. They are generators of continuous symmetry transformations, the time translation, and the rotation. For a full circle M_2, we can find energy eigenstates which are simultaneous eigenstates of $\hat{H}_2$ and $\hat{p}_\theta$,

$$\langle \mathbf{r}|l,k\rangle^{(f)} \propto J_l\left(\frac{\alpha_{lk}r}{R}\right)e^{il\theta}, \tag{9}$$

where k is a positive integer, l is an integer, and α_{lk} is the kth zero of the Bessel function $J_l(x)$. And energy levels are given by $E_{lk}^{(f)}=\hbar^2\alpha_{lk}^2/(2mR^2)$. There exist twofold degeneracies when $l\neq 0$ since the system also has the parity symmetry and $[\hat{p}_\theta,\hat{P}]\neq 0$ ($\hat{P}$ is the parity operator). Then we can find another set of energy eigenstates, simultaneous eigenstates of $\hat{H}_2$, $\hat{p}_\theta^2$, and $\hat{P}$,

$$\begin{aligned}\langle \mathbf{r}|l,k,+\rangle^{(f)} &\propto J_l\left(\frac{\alpha_{lk}r}{R}\right)\cos(l\theta) \quad (l\geq 0),\\ \langle \mathbf{r}|l,k,-\rangle^{(f)} &\propto J_l\left(\frac{\alpha_{lk}r}{R}\right)\sin(l\theta) \quad (l\geq 1),\end{aligned} \tag{10}$$

where $-\pi<\theta<\pi$. The latter will be used in the calculation of the quantum web.

For a half circle M_1, energy levels are the same as those of the full circle without levels with $l=0$, and the energy eigenfunctions are

$$\begin{aligned}\langle \mathbf{r}|l,k,+\rangle^{(h)} &\propto J_l\left(\frac{\alpha_{lk}r}{R}\right)\cos(l\theta) \quad (l=1,3,5,\ldots),\\ \langle \mathbf{r}|l,k,-\rangle^{(h)} &\propto J_l\left(\frac{\alpha_{lk}r}{R}\right)\sin(l\theta) \quad (l=2,4,6,\ldots),\end{aligned} \tag{11}$$

where $-\pi/2<\theta<\pi/2$. Here there is no degeneracy.

For classically nonintegrable cases, $\hat{p}_\theta^2$ no longer commutes with $\hat{H}_w$ (but still $[\hat{P},\hat{H}_w]=0$ for any w). Here Eq. (8) must be solved numerically. We use the boundary element method (BEM) [2,21–23] to solve this nonseparable 2D partial differential equation. It is an efficient way to solve boundary-value problems, because in the BEM a 2D equa-

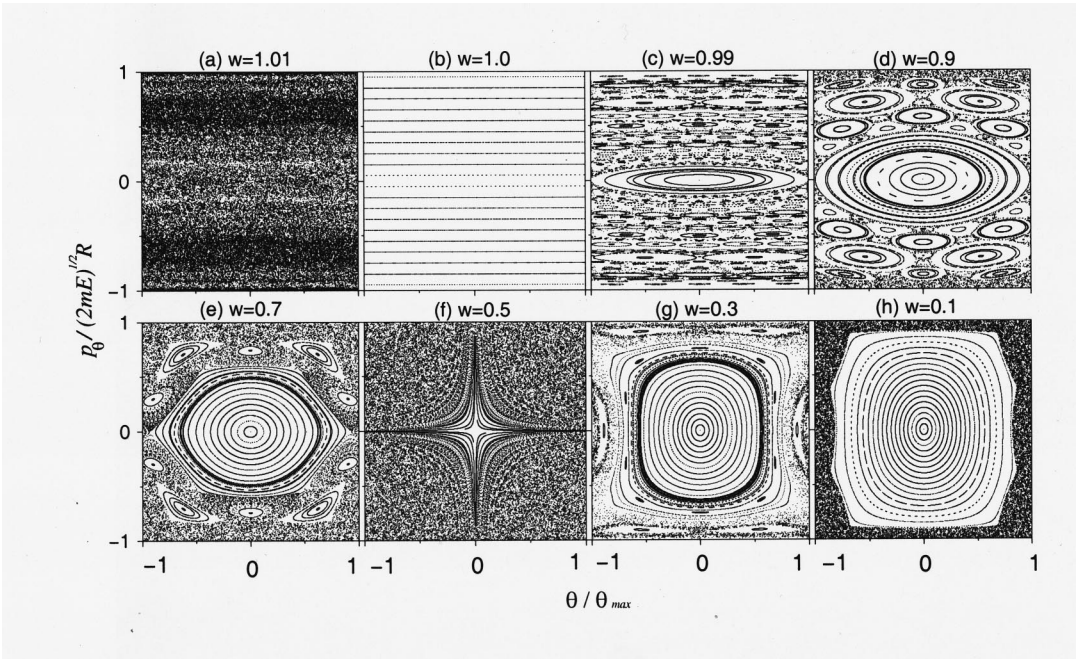

FIG. 4. Poincaré surface of section of M_w billiard varying w, where $w=W/R$. We observe ergodic motions when $1<w<2$ and generic chaotic behaviors when $0<w<1$. (a) Ergodic when $w=1.01$ with one orbit. (b) Integrable when $w=1$. (c) $w=0.99$. (d) $w=0.9$. (e) $w=0.7$. (f) $w=0.5$. Closed orbits residing in ($\theta=0$) axis and ($p_\theta=0$) axis have neutral stabilities. One orbit is filling almost all of the space except for two axes. (g) $w=0.3$. (h) $w=0.1$.

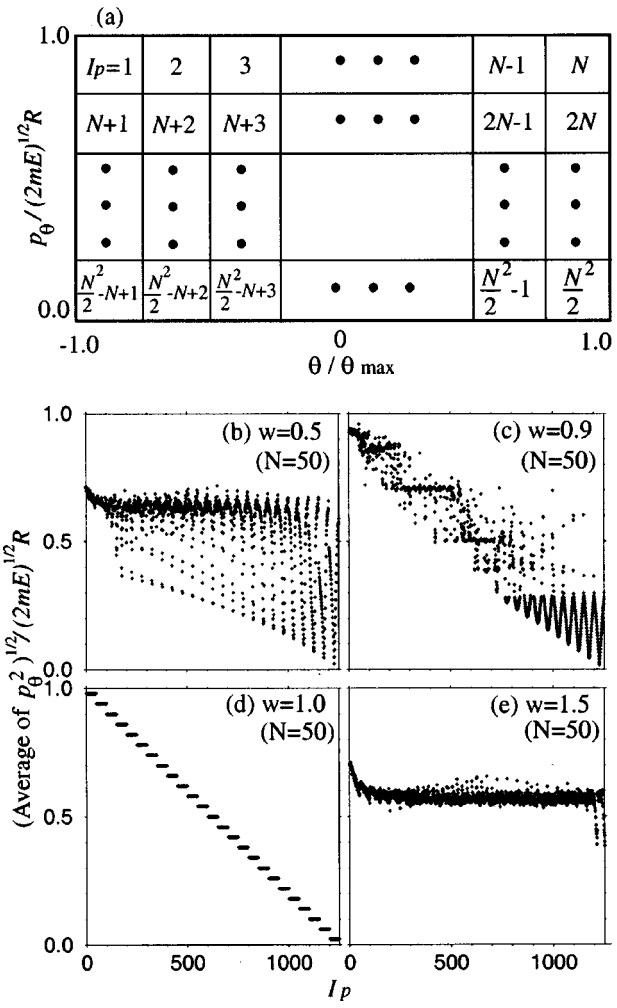

FIG. 5. Finding finite-time averages of p_θ^2. (a) The upper half of the Poincaré surface of section, which is divided into $N^2/2$ blocks, and each block is numbered by I_p. For each block, the root mean square of p_θ at the circular boundary for a finite time can be calculated. (b) $w=0.5$. (c) $w=0.9$. (d) $w=1.0$. (e) $w=1.5$.

tion with boundary condition becomes an integral equation in one variable along the boundary. The method we use is briefly outlined below.

We use a Green's function, $G(\mathbf{r},\mathbf{r}')=-(i/4)H_0^{(1)}(k|\mathbf{r}-\mathbf{r}'|)$, which satisfies

$$(\nabla^2+k^2)G(\mathbf{r},\mathbf{r}')=\delta(\mathbf{r}-\mathbf{r}'), \tag{12}$$

where $H_i^{(1)}(x)$ is the Hankel function of the first kind. We multiply Eq. (8) by $G(\mathbf{r},\mathbf{r}')$, and multiply Eq. (12) by $\Psi(\mathbf{r}')$. After subtracting one from the other, integrating over the area of M_w with respect to $\mathbf{r}'$, and using Green's theorem, we finally get

$$-\oint_{B_w} ds' G(\mathbf{r},\mathbf{r}')u(s')=\begin{cases}\Psi(\mathbf{r}), & \mathbf{r} \text{ inside } B_w,\\ \frac{1}{2}\Psi(\mathbf{r}), & \mathbf{r} \text{ on } B_w,\\ 0, & \mathbf{r} \text{ outside } B_w,\end{cases} \tag{13}$$

where s' is the arc length along $B_w=\partial M_w$, $u(s')$ is defined by $\mathbf{n}'\cdot\nabla'\Psi(\mathbf{r}(s'))$, and $\mathbf{n}'$ is the outward normal unit vector to B_w at $\mathbf{r}'$. With $\mathbf{r}$ lying on B_w, by taking the normal derivative $\mathbf{n}\cdot\nabla$ on both sides of Eq. (13), we obtain

$$u(s)=-2\oint_{B_w} ds' u(s')(\mathbf{n}\cdot\nabla)G(\mathbf{r},\mathbf{r}'). \tag{14}$$

One way to solve this equation is discretizing B_w by dividing it into N segments. Then Eq. (14) becomes a matrix equation $\mathbf{A}\cdot\mathbf{x}=\mathbf{x}$, where $\mathbf{A}=\mathbf{A}(k)$ is an $(N\times N)$ matrix and $\mathbf{x}$ is an N-component vector representing $\{u(s_i)|1\leqslant i\leqslant N\}$. For given w, energy levels of the system, $E_n=\hbar^2k_n^2/2m$ $(n\geqslant 1)$, can be found by solving the equation, $\det|\mathbf{A}(k)-\mathbf{I}|=\mathbf{0}$. For each energy level E_n, we can obtain $\{u_n(s_i)\}$ by finding an eigenvector of $\mathbf{A}(k_n)-\mathbf{I}$ with a near-zero eigenvalue. Since the numerically obtained energy levels in this way always have some uncertainty, ''degeneracy'' (which is actually near-degeneracy) can occur when the difference between two adjacent exact energy levels is less than the uncertainty. In these cases, we can find two sets of $\{u(s_i)\}$ with two near-zero eigenvalues of $\mathbf{A}$. Therefore, looking at eigenvalues of $\mathbf{A}(k_n)$ can be an easy way to check numerically for near-degeneracies of an energy level, E_n.

For given w, we found energy levels $\{E_n|n\geqslant 1\}$ and normal derivatives, on the boundary, of corresponding energy eigenfunctions $\{\Psi_n(\mathbf{r})\equiv\langle\mathbf{r}|n\rangle\}$, where $|n\rangle$'s are energy eigenstates. Then from Eq. (13) we can calculate the energy eigenfunction inside,

$$\Psi_n(\mathbf{r})=\frac{i}{4}\oint_{B_w} ds' H_0^{(1)}(k_n|\mathbf{r}-\mathbf{r}'|)u_n(s'). \tag{15}$$

Using Eq. (15), we can also calculate $\langle\mathbf{r}|\hat{p}_\theta^2|n\rangle$, which will be used in calculations of quantum webs in the next subsection,

$$\begin{aligned}\langle\mathbf{r}|\hat{p}_\theta^2|n\rangle&=-\hbar^2\frac{\partial^2}{\partial\theta^2}\Psi_n(\mathbf{r})\\&=\frac{i}{4}\oint_{B_w} ds'\left[\frac{\partial^2}{\partial\theta^2}H_0^{(1)}(k_n|\mathbf{r}-\mathbf{r}'|)\right]u_n(s'),\end{aligned} \tag{16}$$

where

$$\begin{aligned}\frac{\partial^2}{\partial\theta^2}H_0^{(1)}(k|\mathbf{r}-\mathbf{r}'|)&=k\left[\frac{\partial^2}{\partial\theta^2}\left|\mathbf{r}-\mathbf{r}'\right|\right]H_0^{(1)\prime}(k|\mathbf{r}-\mathbf{r}'|)\\&\quad+k^2\left[\frac{\partial}{\partial\theta}\left|\mathbf{r}-\mathbf{r}'\right|\right]^2H_0^{(1)\prime\prime}(k|\mathbf{r}-\mathbf{r}'|),\end{aligned} \tag{17}$$

and we use

$$|\mathbf{r}-\mathbf{r}'|=\sqrt{(r\cos\theta-x')^2+(r\sin\theta-y')^2}, \tag{18}$$

and

$$\begin{aligned}H_0^{(1)\prime}(x)&=-H_1^{(1)}(x),\\H_0^{(1)\prime\prime}(x)&=-H_0^{(1)}(x)+H_1^{(1)}(x)/x.\end{aligned} \tag{19}$$

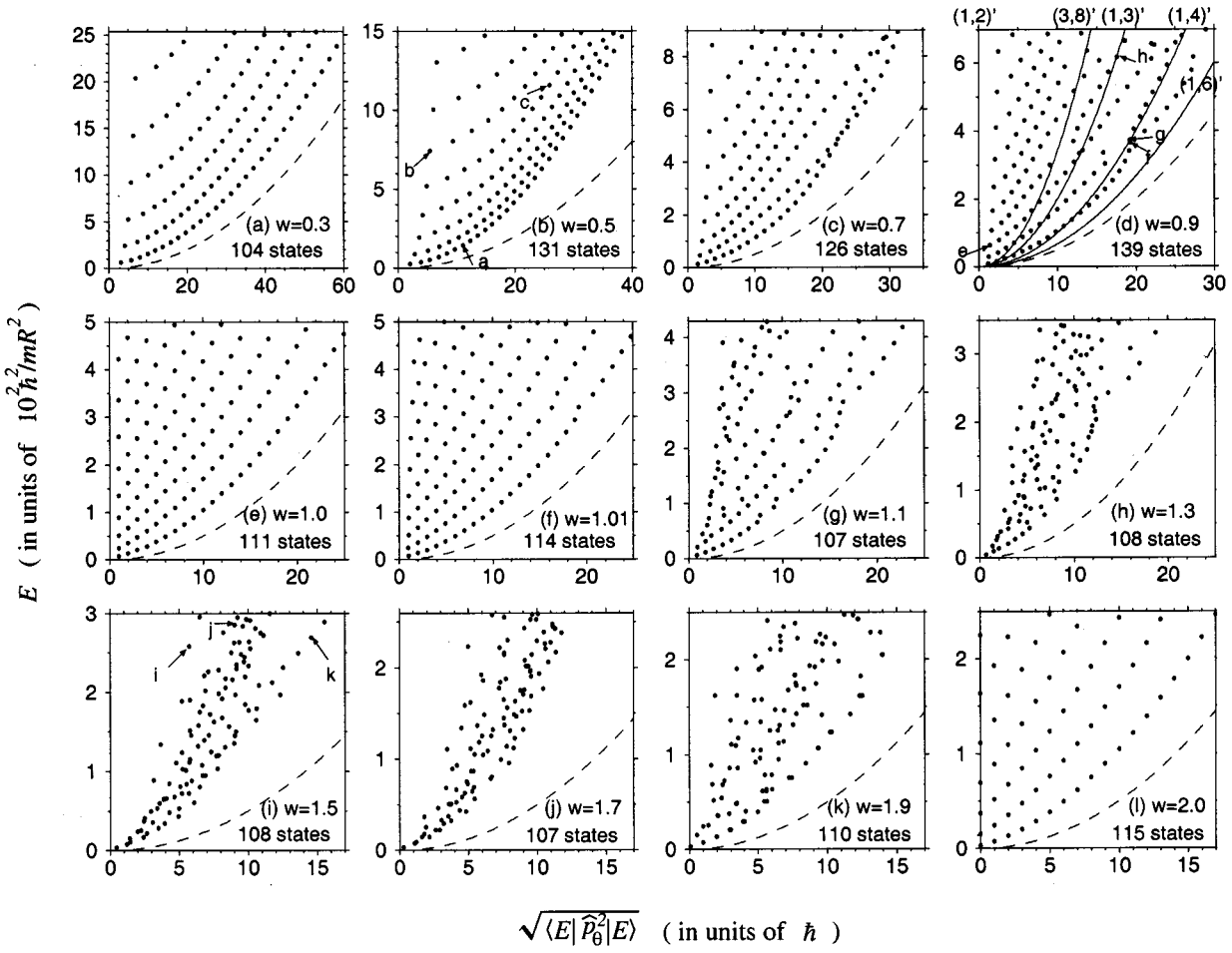

FIG. 6. Quantum web of M_w billiard varying w. Even and odd parity eigenstates are shown together. (a) $w=0.3$. (b) $w=0.5$. (c) $w=0.7$. (d) $w=0.9$. The conditions for primary resonances in classical mechanics are also shown. (e) $w=1.0$. Classically integrable case. (f) $w=1.01$. (g) $w=1.1$. (h) $w=1.3$. (i) $w=1.5$. (j) $w=1.7$. (k) $w=1.9$. (l) $w=2.0$. Classically integrable case. There are twofold degeneracies when $p_\theta \neq 0$. [The arrows in (b), (d), and (i) indicate states that will be studied using Husimi plots in Fig. 7. Outside dashed lines are classically forbidden regions.]

In calculations of Ψ_n and $(\partial^2/\partial\theta^2)\Psi_n$, care must be taken when $\mathbf{r}$ is close to the boundary because $H_i^{(1)}(|\mathbf{r}-\mathbf{r}'|)$ diverges as $|\mathbf{r}-\mathbf{r}'|$ goes to zero.

B. The quantum web

The quantum-web analysis can be used to observe the manifestation of classical chaos in quantum mechanics. Until now the quantum web has been used primarily in spin systems [15,16]. We will construct quantum webs for three different cases: classically integrable cases ($w=1,2$), nonintegrable cases showing soft chaos ($0<w<1$), and nonintegrable cases with hard chaos ($1<w<2$).

For classically integrable cases ($w=1,2$), we have seen in Sec. II that there are two constants of motion, E and $|p_\theta|$, and that we can find two action variables (J_r, J_θ). [There exists a nonlinear map from (J_r, J_θ) space to $(E,|p_\theta|)$ space.] In Fig. 3, a classical orbit appears as a point in $(E,|p_\theta|)$ space. In quantum mechanics, there exist simultaneous eigenstates of two operators $\hat{H}_w(w=1$ or 2) and $\hat{p}_\theta^2$ [see Eqs. (10) and (11)]. We can construct a 2D space, in which a pair of eigenvalues $(E_{lk}, |l\hbar|)$ of each eigenstate is plotted as a point. In Figs. 6(e) and 6(l), we observe the structure of a deformed lattice. This can be understood as a mapping from an almost perfect 2D square lattice in (J_r, J_θ) space to the deformed lattice in $(E,|p_\theta|)$ space. This almost perfect lattice structure can be explained from Einstein-Brillouin-Keller (EBK) semiclassical quantization,

$$J_r \simeq (n_r - \tfrac{1}{4})\hbar \quad (n_r: \text{positive integer}),$$
$$J_\theta = p_\theta = l\hbar \quad (l: \text{integer}), \tag{20}$$

where J_r is a very good approximation and J_θ is exact. This is the quantum analog of Fig. 3 in which each point represents a 2-torus. Thus, we can find a 2-torus in classical phase space corresponding to a quantum eigenstate, and then each eigenstate here corresponds to a set of orbits that are on this 2-torus.

For classically nonintegrable cases, $[\hat{p}_\theta^2, \hat{H}_w] \neq 0$ when $w \neq 1$ or 2. We can still calculate an expectation value of $\hat{p}_\theta^2$ for an energy eigenstate $|n\rangle$, $\langle n|\hat{p}_\theta^2|n\rangle$, numerically using Eqs. (15) and (16),

$$\langle n|\hat{p}_\theta^2|n\rangle = \int_{M_w} d^2\mathbf{r}\langle n|\mathbf{r}\rangle\langle\mathbf{r}|\hat{p}_\theta^2|n\rangle$$

$$= -\hbar^2 \int_{M_w} d^2\mathbf{r}\,\Psi_n^*(\mathbf{r})\frac{\partial^2\Psi_n(\mathbf{r})}{\partial\theta^2}. \qquad (21)$$

These values can be interpreted as time averages of $\hat{p}_\theta^2$ [14]. When there is an accidental degeneracy (or near-degeneracy), we find expectation values from eigenvalues of the matrix representation of $\hat{p}_\theta^2$ in the degenerate subspace. In this way, we obtain a pair of values $(E_n, \sqrt{\langle n|\hat{p}_\theta^2|n\rangle})$ for each energy eigenstate. These points can also be plotted in a 2D space as a quantum web. We expect lattice structures that exist for integrable cases will be broken because EBK quantization does not apply to nonintegrable cases.

In Figs. 6(a)–6(d), quantum webs are shown for cases of soft chaos. When $w=0.99$ [Fig. 6(d)], we observe breaking of the web near conditions of primary resonances in classical mechanics. We see patterns of crossing near $(1,4)'$ and $(1,3)'$ resonances. Although ''regular'' parts still exist, some layers seem to start to shift near resonance conditions. We can roughly estimate the energy value at which the effect starts to be seen for each resonance condition by measuring the width of island chains, Δp_θ, in Fig. 4(d). For example, $(1,2)'$ resonance has the biggest width, the next $(1,4)'$ resonance, and so on. Because p_θ is scaled by $(R\sqrt{2mE})^{-1}$ in Fig. 4, Δp_θ is proportional to $\sqrt{E}$. When $\Delta p_\theta (=\Delta J_\theta) \geq \hbar$, the resonance can be clearly seen in the quantum system, and we can roughly obtain an estimate of the minimum energy at which each resonance is in effect. The smaller the width of an island chain and the lower the energy, the less likely to find the web broken near the curve of the particular resonance. When $w=0.7$ [Fig. 6(c)], we see similar patterns as in Fig. 6(d). When $w=0.5$ [Fig. 6(b)], the classical system has a large chaotic region in the PSS, and has periodic orbits with neutral stability, which reside on two axes, $\theta=0$ and $p_\theta=0$. The quantum web, however, is quite regular although the structure looks different from those of integrable cases. It looks more like a structure of layers. When $w=0.3$ [Fig. 6(a)], the web is similar to that of Fig. 6(b).

In Figs. 6(f)–6(k), we show quantum webs for cases of hard chaos. When $w=1.01$ [Fig. 6(f)], the lattice structure is still intact except a little kink, although this is the fully chaotic case classically [see Fig. 4(a)]. For these low energies, the quantum system does not see the broken symmetry well, because the wavelengths of the eigenstates are longer than the deviations of the width from the half-circle. We observe that the lattice structure quickly collapses as we increase w. When $w=1.5$ [Fig. 6(i)], the structure is very irregular except for four regularly placed points near the top-right corner. (Some of the eigenstates noted by arrows here will be examined in the next subsection using Husimi plots.) The case of $w=1.7$ [Fig. 6(j)] is the most irregular quantum web among cases shown. When $w=1.9$ [Fig. 6(k)], we observe splitting of degeneracies and also quick collapse of lattice structure from an integrable case $w=2$ [Fig. 6(l)]. As we have seen so far, the lattice structure tends to collapse quickly in cases of hard chaos, but there also exist small remnants of regularity in some cases.

We can relate the finite-time averages of classical p_θ^2 shown in Fig. 5 to quantum webs in Fig. 6. Energy was scaled away in classical mechanics unlike in the quantum web, where energy plays an important role. But classical results can still help us to understand quantum webs better. For cases of hard chaos, we can explain why the points in quantum webs [Figs. 6(f)–6(l)] are squeezed into a small range, because classically $\langle p_\theta^2\rangle$ approaches one value regardless of initial conditions as we saw in Fig. 5(e). For cases of soft chaos, quantum webs [Figs. 6(a)–6(d)] can have distinct regular and irregular regions as in Figs. 5(b) and 5(c). These qualitative features are expected to remain even in higher energies.

C. Quantum Poincaré section

The Husimi plot provides a method of extracting a quantum Poincaré surface of section (QPS) from a quantum state [17]. The QPS is a quantum analog of PSS, which we have obtained in Sec. II. The Husimi function of a 1D system corresponding to a state $|\Psi\rangle$ is defined as

$$F(x_0,p_0) = |\langle x_0,p_0|\Psi\rangle|^2, \qquad (22)$$

where $|x_0,p_0\rangle$ is a coherent state with a representation in configuration space,

$$\langle x|x_0,p_0\rangle = \left(\frac{1}{\pi\sigma^2}\right)^{1/4} \exp\left[-\frac{(x-x_0)^2}{2\sigma^2} + \frac{i}{\hbar}p_0(x-x_0)\right]. \qquad (23)$$

In 2D billiards, Eq. (22) can be modified to create a Husimi function using the coordinate along the boundary [18]. For example, for M_w billiard along the circular part of the boundary, the Husimi function is defined as

$$F_n(\theta_0,p_{\theta 0}) = \left|\int_{-\theta_{\max}}^{\theta_{\max}} d\theta' \langle\theta_0,p_{\theta 0}|\theta'\rangle u_n(\theta')\right|^2, \qquad (24)$$

where $-\theta_{\max} < \theta_0 < \theta_{\max}$ and $-R\sqrt{2mE} < p_{\theta 0} < R\sqrt{2mE}$. Here $\langle\theta'|\theta_0,p_{\theta 0}\rangle$ has the same form as in Eq. (23) with σ given by the value $[\theta_{\max}\hbar/(R\sqrt{2mE})]^{1/2}$, and $u_n(\theta)$ is the normal derivative of the energy eigenfunction on the circular part of the boundary, $(\partial/\partial r)\Psi_n(\mathbf{r})|_{r=R}$.

In Fig. 7, we show Husimi plots for selected eigenstates for three cases $(w=0.5,0.9,1.5)$. And, in Fig. 8, we show probability densities of wave functions, $|\Psi_n(\mathbf{r})|^2$, for some of the eigenstates chosen from Fig. 7. [Most eigenstates chosen in Fig. 7 can be found in Figs. 6(b), 6(d), and 6(i) with arrows pointed to them.]

Figures 7(a)–7(d) show Husimi plots of energy eigenstates when $w=0.5$. The pattern of PSS shown in Fig. 4(f) can be seen in these plots. We can get some information on chosen eigenstates from the quantum web [Fig. 6(b)]. The eigenstate for Fig. 7(a) is on the outer part, and the eigenstate for Fig. 7(b) is on the inner part of the quantum web. Figure 7(a) shows the chaotic region of PSS, and Fig. 7(b) seems to correspond with a two-bounce orbit with neutral stability, which we can observe in the wave function [Fig. 8(a)]. The eigenstate for Fig. 6(c) is in the middle of the quantum web, and its Husimi plot and wave function [Fig. 7(b)] lie between

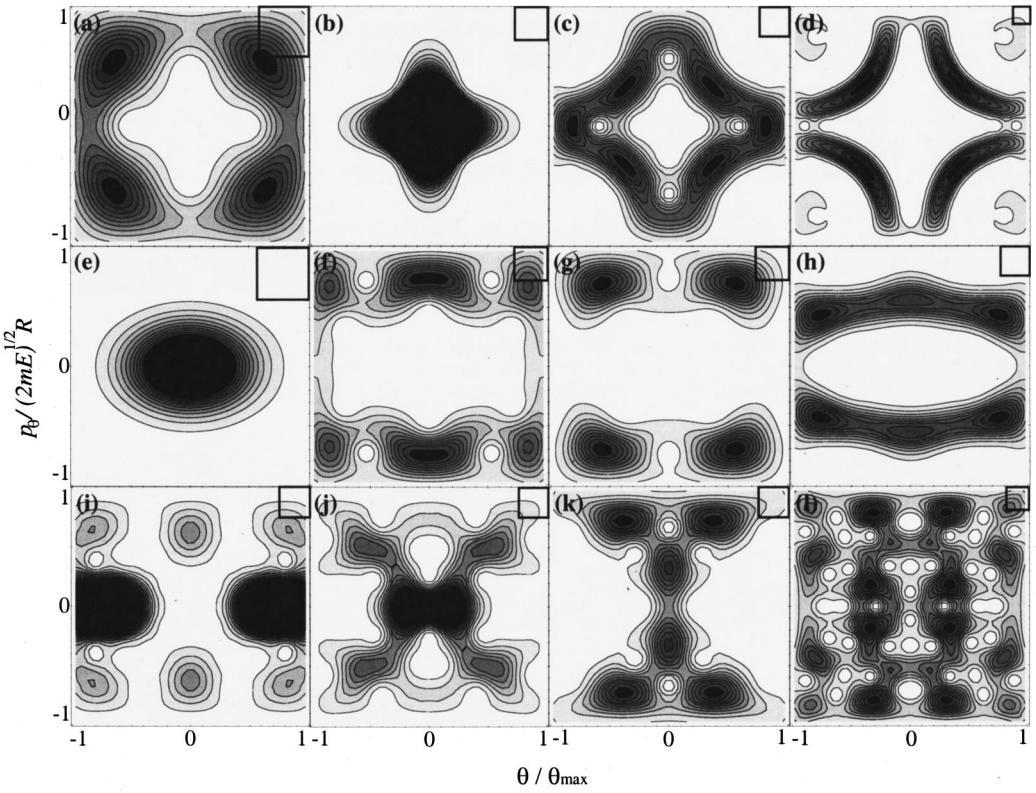

FIG. 7. Husimi plots for given eigenstates [$\epsilon \equiv E/(\hbar^2/mR^2)$]. (a) $w=0.5$ and $\epsilon=143.28$. (b) $w=0.5$ and $\epsilon=740.79$. (c) $w=0.5$ and $\epsilon=1156.07$. (d) $w=0.5$ and $\epsilon=9992.23$. (e) $w=0.9$ and $\epsilon=62.513$. (f) $w=0.9$ and $\epsilon=365.64$. (g) $w=0.9$ and $\epsilon=371.99$. (h) $w=0.9$ and $\epsilon=617.98$. (i) $w=1.5$ and $\epsilon=258.03$. (j) $w=1.5$ and $\epsilon=284.94$. (k) $w=1.5$ and $\epsilon=268.80$. (l) $w=1.5$ and $\epsilon=842.69$. [A square at the top right corner of each plot represents the size of h (Planck constant). All eigenstates except (d) and (l) are pointed in quantum webs in Fig. 6 by arrows.]

two extreme cases above. The eigenstate for Fig. 6(d) has a relatively high energy, but the structure is similar to Fig. 6(c).

Figures 7(e)–7(h) show Husimi plots of energy eigenstates when $w=0.9$, and each eigenstate is picking up a classical primary resonance shown as an island chain in PSS [Fig. 4(d)]. The eigenstate for Fig. 7(e), located near the $(1,2)'$ resonance in the quantum web [Fig. 6(d)], shows the pattern of the island chain of the $(1,2)'$ resonance, although it is only the ninth highest energy eigenstate. The eigenstates of Figs. 7(f) and 7(g), located at the crossing of two layers near the $(1,4)'$ resonance, show the pattern of the island chain of the $(1,4)'$ resonance. Wave functions [Figs. 8(c) and 8(d)] of these states show the trace of unstable and stable periodic orbits [see Fig. 2(b)], respectively. The eigenstate for Fig. 7(h), which is on the $(1,3)'$ resonance, also shows the pattern of the island chain of the $(1,3)'$ resonance. As expected earlier, the $(1,2)'$ resonance is observed in the Husimi plot at lower-energy eigenstates than the $(1,4)'$ resonance.

Figures 7(i)–7(l) show Husimi plots of energy eigenstates when $w=1.5$. The eigenstate for Fig. 7(i), located in the inner part of the quantum web [Fig. 6(i)], seems to be picking up the periodic orbit with neutral stability, which can be clearly seen in the wave function [Fig. 8(e)]. The eigenstate of Fig. 7(k), which is one of four regularly placed points in the quantum web, shows a *whispering gallery* state [Fig. 8(f)]. All four of these regularly placed eigenstates show

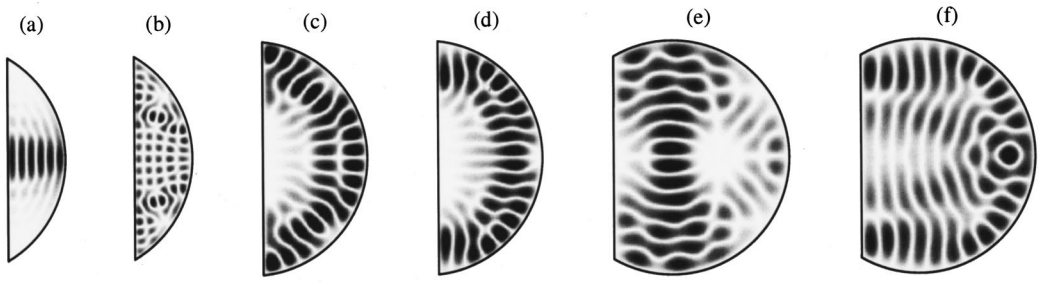

FIG. 8. Probability density of some energy eigenstates [$\epsilon \equiv E/(\hbar^2/mR^2)$]. (a) $w=0.5$ and $\epsilon=740.79$. [See Fig. 7(b).] (b) $w=0.5$ and $\epsilon=1156.07$. [See Fig. 7(c).] (c) $w=0.9$ and $\epsilon=365.64$. [See Fig. 7(f).] (d) $w=0.9$ and $\epsilon=371.99$. [See Fig. 7(g).] (e) $w=1.5$ and $\epsilon=258.03$. [See Fig. 7(i).] (f) $w=1.5$ and $\epsilon=268.80$. [See Fig. 7(k).]

similar Husimi plots. A relatively high energy eigenstate for Fig. 7(l) shows a more uniformly distributed Husimi plot like the corresponding PSS in classical mechanics.

IV. CONCLUSIONS

We studied classical and quantum chaos of a circular billiard with a straight cut. First, we studied the classical system. Since we are only interested in trajectories (orbits), the energy of the particle is unimportant. Periodic orbits of integrable cases were found, and PSS's were plotted for several w's. Nonintegrable cases showed both hard chaos ($1<w<2$) and soft chaos ($0<w<1$). In the quantum system, the energy plays an important role. At higher energies, we are more likely to see the quantum manifestations of classical chaos, because the higher the energy, the smaller the size of h (Planck constant) in the scaled quantum Poincaré section. We calculated quantum webs numerically. Although about 100 states were used here (the cost of calculating the quantum web increases rapidly with energy), they were enough to show different behaviors of hard and soft chaos. In the regime of soft chaos ($0<w<1$), we observed that the lattice-like structure obtained for an integrable case ($w=1$) starts to break, as w decreases, near the primary-resonance conditions obtained from classical mechanics. However, there remained interesting patterns such as layers. The higher the energy and the larger the width of an island chain in PSS, the greater the effect of resonances. For the special case ($w=0.5$), layer structure clearly remained in the low-energy regime we observed. In the hard-chaos regime ($1<w<2$), the regular quantum web collapses more quickly as w changes from integrable cases ($w=1,2$). There was no distinct layer structure when the system was far from integrable except for a few small regularities as seen in Fig. 6(i). [Corresponding states in this particular regularity seem to be related to ''scars.'' As we observe Fig. 7(k) and Fig. 8(f), those states correspond to an unstable periodic orbit that looks similar to $(1,6)'$ in Fig. 2(b).] Even though soft and hard chaos do not manifest themselves as clearly as in classical mechanics, we were able to observe qualitative differences for both cases.

The authors believe that the quantum web, which has been studied primarily in spin systems so far, is a useful technique to understand the quantum chaos in 2D billiards, since we can observe not only the energy eigenvalues but also the eigenfunctions through expectation values of another operator. It also shows distinct patterns for three different cases (integrable, soft chaos, and hard chaos).

ACKNOWLEDGMENTS

The authors wish to thank the Welch Foundation under Grant No. F-1051, the NSF under Grant No. INT-9602971, and the U.S. DOE under Contract No. DE-FG03-94ER14405 for partial support of this work. We thank NPACI and the University of Texas High Performance Computing Center for use of its facilities.

[1] M. V. Berry, Eur. J. Phys. **2**, 91 (1981).
[2] M. V. Berry and M. Wilkinson, Proc. R. Soc. London, Ser. A **392**, 15 (1984).
[3] M. Robnik, J. Phys. A **17**, 1049 (1984).
[4] M. V. Berry, Ann. Phys. (N.Y.) **131**, 163 (1981).
[5] S. W. McDonald and A. N. Kaufman, Phys. Rev. Lett. **42**, 1189 (1979); Phys. Rev. A **37**, 3067 (1988).
[6] E. J. Heller, Phys. Rev. Lett. **53**, 1515 (1984).
[7] M. C. Gutzwiller, *Chaos in Classical and Quantum Mechanics* (Springer-Verlag, New York, 1990).
[8] G. O. Morrow and L. E. Reichl, Phys. Rev. A **50**, 2027 (1994).
[9] S. Ree and L. E. Reichl, Phys. Rev. E **55**, 2409 (1997).
[10] I. C. Percival, J. Phys. B **6**, L229 (1973).
[11] M. V. Berry and M. Tabor, Proc. R. Soc. London, Ser. A **356**, 375 (1977).
[12] O. Bohigas, M. J. Giannoni, and C. Schmit, Phys. Rev. Lett. **52**, 1 (1984).
[13] L. E. Reichl, *The Transition to Chaos in Conservative Classical Systems: Quantum Manifestations* (Springer-Verlag, New York, 1992).
[14] A. Peres, Phys. Rev. Lett. **53**, 1711 (1984).
[15] N. Srivastava and G. Müller, Z. Phys. B **81**, 137 (1990); N. Srivastava, C. Kaufman, and G. Müller, J. Appl. Phys. **67**, 5627 (1990).
[16] D. T. Robb and L. E. Reichl, Phys. Rev. E **57**, 2458 (1998).
[17] K. Husimi, Proc. Phys. Math. Soc. Jpn. **22**, 246 (1940).
[18] B. Crespi, G. Perez, and S. J. Chang, Phys. Rev. E **47**, 986 (1993).
[19] E. J. Heller and S. Tomsovic, Phys. Today **46** (7) 38 (1993).
[20] L. A. Bunimovich, Commun. Math. Phys. **65**, 295 (1979); Funct. Anal. Appl. **8**, 73 (1974).
[21] G. R. C. Tai and R. P. Shaw, J. Acoust. Soc. Am. **56**, 796 (1974).
[22] N. Kishi and T. Okoshi, IEEE Trans. Microwave Theory Tech. **MTT-35**, 887 (1987).
[23] P. A. Knipp and T. L. Reinecke, Phys. Rev. B **54**, 1880 (1996).